Total cross section and neutron resonance spectroscopy for $n + {}^{40}$Ar

R. R. Winters
Denison University, Granville, Ohio 43023

R. F. Carlton
Middle Tennessee State University, Murfreesboro. Tennessee 37132

C. H. Johnson and N. W. Hill
Oak Ridge National Laboratory, Oak Ridge, Tennessee 37831

M. R. Lacerna
Ohio State University, Columbus, Ohio 43210
(Received 27 August 1990)

The neutron total cross section for ^{40}Ar has been measured over the incident neutron energy range 0.007–50 MeV. R-matrix analysis of the cross section from 0.007 to 1.52 MeV provides resonance parameters which provide a complete description of the neutron scattering functions for the $s_{1/2}, p_{1/2}$, and $p_{3/2}$ scattering channels and less nearly complete scattering functions for the $d_{3/2}$ and $d_{5/2}$ channels. The back-shifted Fermi-gas model is used to model the level densities for s-, p-, and d-wave resonances.

I. INTRODUCTION

Several recent analyses[1-6] have shown that the introduction of the dispersion relation constraint[1] into the parametrization of the neutron-nucleus mean field makes possible good descriptions of empirical data for a broad range of energies from negative energies of the single-particle bound states to positive energies of neutron scattering. This success is due to the important components of the real part of the mean field that are predicted by the dispersion relation from the imaginary components. The neutron-nucleus systems that have been investigated[2-4] so far for broad energy regions are n-^{40}Ca, n-^{90}Zr, and n-^{208}Pb. A common feature of each of these systems is a closed neutron shell: 20 neutrons for ^{40}Ca, 50 for ^{90}Zr, and 128 for ^{208}Pb. Studies[5,6] for more limited energy regions have been made for the n-^{89}Y and n-^{86}Kr systems, both of which also have closed 50-neutron shells.

The present paper is devoted to measurements and analysis of empirical data in the resolved resonance region, which extends upward about 1.5 MeV from the neutron separation energy. A unique feature of this region is that scattering functions for individual partial waves can be obtained by an R-matrix analysis of the observed resonance structure. Since the "dispersive optical model" provides a good description of data at energies both above and below the resonance region, it can be reasonably expected to describe the energy-average scattering functions for individual partial waves within the region. Indeed, the recent analysis[6] for n-^{86}Kr showed for that system that extrapolation of the mean field from higher energies provides a very good description of the averaged empirical scattering functions.

Here we report experimental measurements and an R-matrix analysis for the neutron total cross section of ^{40}Ar for energies from 0.007 to 1.5 MeV. In addition, we report energy-averaged total cross sections for neutron energies above the resonance region up to 50 MeV. A significant fact is that ^{40}Ar does not have a closed neutron shell; it has 22 neutrons with two of the neutrons in the $1f_{7/2}$ shell outside the 20-neutron shell. The question arises as to whether or not the dispersive optical model[2] that works so well for the doubly closed shell ^{40}Ca nucleus can be extended to ^{40}Ar by the simple addition of small isovector potential contributions.

Accurate determination of the optical model potential in the resonance region requires very good energy resolution such that statistically significant numbers of resonances can be resolved and analyzed. Ideally, the resolution should be good enough to allow the analysis to extend up to the neutron inelastic threshold because below that threshold the R matrix reduces to an R function which can be evaluated with little uncertainty. The inelastic threshold for ^{40}Ar is 1.5 MeV. The only previous high-resolution measurements[7,8] of the ^{40}Ar neutron total cross section were made at the Columbia University Nevis synchro-cyclotron[7] for energies up to 0.58 MeV and at the Duke University Nuclear Structure Laboratory[8] up to 0.65 MeV. Here we make use of the better energy resolution available at the Oak Ridge Electron Linear Accelerator (ORELA), and, indeed, are able to extend the analysis upward to the inelastic threshold at 1.5 MeV.

Our paper is organized as follows. In Sec. II we describe the measurements, and in Sec. III we present the resulting total cross sections for neutrons on ^{40}Ar. In Sec. IV we briefly review the R-matrix formalism, and in Sec. V we describe the process of determining the R functions and strength functions from the observed cross sections and report the resulting resonance and off-resonance parameters. These parameters provide an

essentially complete description of the scattering functions for the first few partial waves, and they are the input to the dispersive optical model analysis, which is to be presented in a subsequent paper. Section VI is a statistical analysis of the resonance parameters and Sec. VII is our conclusion.

II. MEASUREMENTS

A. Neutron source, detectors, and argon sample

The Oak Ridge Electron Linear Accelerator[9,10] (ORELA) was used to produce a pulsed neutron beam by bombarding a Be-clad, water-moderated tantalum target with electrons in bursts of 7 nsec with a repetition rate of 800 pps. The neutron detector was a NE110 scintillator coupled to an 8854 RCA photomultiplier. The scintillator was a cylinder 8.89 cm in diameter and 2.3 cm thick in the beam direction. Four separate pulse-height spectra were recorded with differing lower discriminator bias corresponding approximately to 0.0, 0.05, 0.325, and 1.15 MeV neutron energies. These bias groups facilitate corrections for various background events and for afterpulsing in the detector due to the intense burst of gamma radiation associated with each ORELA pulse. The detector was located 201.578 ± 0.003 m from the center of the ORELA neutron source. A fission chamber located approximately 4 m from the ORELA source served as a monitor of the neutron flux emanating from the source.

The transmission sample was pure, 99.97%, natural argon pressurized to about 37 atm in a steel cylinder with 221.6 cm length and 16.14 cm internal diameter. The end caps were 0.34 cm thick spherical sections with 13.5 cm radii. We determined the areal density of the gas along the axis from the mass of the gas and the internal cross-sectional area of the cylinder. To determine the mass we first balanced the evacuated cylinder on a balance designed for precision measurements of heavy samples; we then filled the cylinder with argon and rebalanced using calibrated weights. The mass of the argon gas was 2858.7 g. Small corrections were made, each less than 1%, for effects related to (i) the curvature of the end plates, (ii) extraneous argon in a small external filling manifold, and (iii) slow leakage during the seven days of the transmission experiment. The corrected areal density was 0.211 atom/b.

For the transmission measurements we placed the cylinder in the neutron flight path 80 m from the ORELA source with its axis aligned with the neutron beam axis. Since the cylinder diameter was more than twice that of the beam diameter, it was easily aligned to ensure against scattering from the walls. We measured the transmission of argon by repeatedly interchanging the argon-filled cylinder with an identical evacuated cylinder. Normally such cycling between a scatterer and its compensator is performed at ORELA under computer control, but in the present experiment the large size of the scatterer and compensator made it necessary to alternate manually. During the seven contiguous days of the measurements, we made 83 argon-compensator cycles with each cycle consisting of about 60 min for the argon scatterer and 45 min for the compensator. We know that the compensation for attenuation in the steel end caps was successful because, even though the 27-keV s-wave resonance in ^{56}Fe is quite pronounced in the spectra for the sample and for its compensator, the resonance is completely absent in the observed transmissions for the argon-compensator cycles.

B. Energy resolution

Two components contribute to the width of the energy resolution function; one is the time width of the ORELA electron beam burst and the other is the fluctuation in neutron flight path. The latter is the combined effect of the path length taken by the neutron from its origin to its exit in the neutron source and the path length within the detector before scattering. The two components can be approximated[11,12] by normal distributions with full widths at half maximum (FWHM) of Δt and ΔL. Combining in quadrature, we have

$$(\Delta E/E)^2 = (2\Delta L/L)^2 + (2\Delta T/T)^2 , \qquad (2.1)$$

where ΔE is the FWHM of the energy resolution function. This equation can be expressed as a linear function of neutron energy,

$$(\Delta E/E)^2 = a + bE . \qquad (2.2)$$

ORELA was tuned to give $\Delta T = 7.0$ nsec. We measured ΔT about every hour during the experiment by examining the time distribution of the γ-ray burst recorded by the detector. We also checked to see that the pulse had a clean shape with negligible satellite pulses. From the 7.0-nsec width and 201-m flight path we calculate the energy coefficient for Eq. (2.2);

$$b = 94 \times 10^{-8} \text{ MeV}^{-1} . \qquad (2.3)$$

For the spatial width ΔL we initially estimated a value of about 4.5 cm on the basis of the 2.3-cm thickness of the detector and the predicted[13] path fluctuations in the source. However, we made our final determination from the experiment itself by fitting isolated transmission dips which are due to resonances that are narrow enough such that the observed widths are nearly ΔE but, at the same time, wide enough to be statistically significant. We found thirteen such minima for $E < 500$ keV and fit them by least squares using five parameters to describe a Breit-Wigner resonance in the cross section superimposed on a linear background. The five parameters were the resonance energy E_λ, the width Γ, the energy resolution width ΔE, and two parameters for the linear background. Since $\Gamma < \Delta E$, the resulting ΔE are insensitive to the assumed peak resonance cross sections. We assume peak cross sections given by $2\pi(2J+1)/k^2$, where k is the neutron wave number and J is the total angular momentum quantum number. The transmission dips are then described using J values of $\frac{1}{2}$, $\frac{3}{2}$, and $\frac{5}{2}$. We also include Doppler broadening of the resonance cross section. In Fig. 1 each vertical line represents the range of best-fit values of ΔE for a resonance. The sloping line has been drawn visually for the best fit under the restriction that
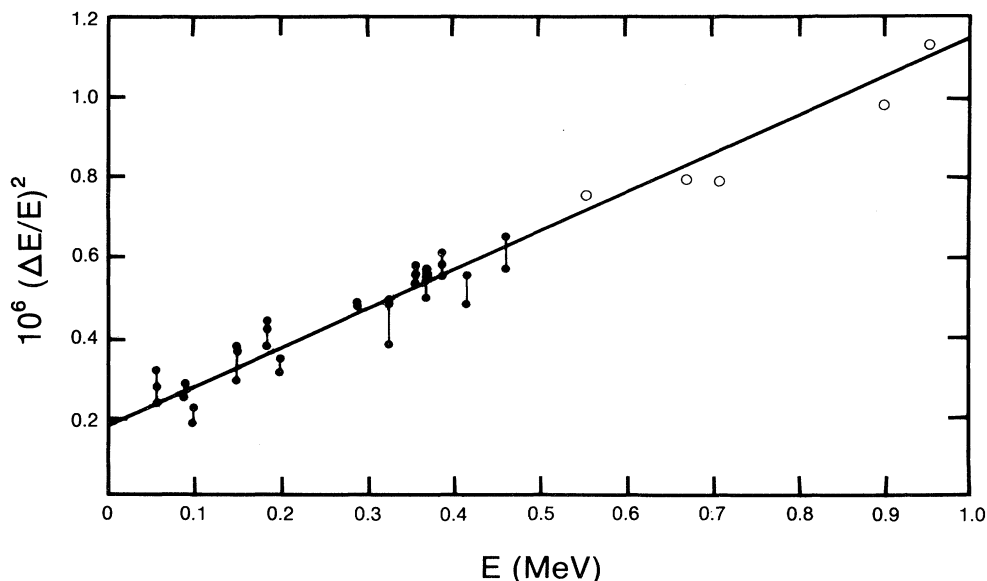
FIG. 1. Fractional resolution width versus neutron energy for the NE110 neutron detector and ORELA neutron source as determined using very narrow isolated resonances. The filled symbols below 500 keV represent the measured $\Delta E/E$ for the three assumed values of J, $\frac{1}{2}$, $\frac{3}{2}$, and $\frac{5}{2}$. The open symbols above 500 keV represent the same quantity but for $J = \frac{1}{2}$ only since, given the uncertainties for each data point, the shapes of these resonances are completely independent of the assumed J.

the slope "b" be given by Eq. (2.3). From this line, we conclude

$$a = 0.18 \times 10^{-6},\qquad(2.4)$$

which corresponds to $\Delta L = 4.2$ cm, in good agreement with the above preliminary estimate. The width ΔL is expected[13] to increase slightly for the higher energies of our analysis, $0.5 < E < 1.5$ MeV. Nevertheless, we use the linear approximation at higher energies because at those energies the contribution to the resolution function from ΔL is small relative to that from ΔT.

Flight-time spectra, each with 70 000 time channels, were recorded for argon and for the compensator time channels. We chose the channel widths to be somewhat smaller than the energy resolution width. For flight times corresponding to $2000 > E > 170$ keV, we used 1-nsec channels; since $\Delta T = 7$ nsec, the 1-nsec width is less than one-seventh of the resolution width. For $70 < E < 170$ keV, we increased the channel width to 2 nsec such that the channel width was $\frac{1}{5}$ to $\frac{1}{7}$ of the resolution width. Below 70 keV we used 4 nsec; this is $1/3.5$ of the resolution width at 70 keV but much less at the lowest energy of about 7 keV. For the purpose of deriving average cross sections over the energy range 2–50 MeV, 1000 channels each 8 ns wide were used.

C. Corrections for deadtime and backgrounds

There are four known sources of background: (1) time-independent room background, (2) 2.2-MeV γ rays from thermal neutron capture in the source moderator water, (3) 478-keV γ rays from the $^{10}B(n,\alpha\gamma)^7Li$ reaction from neutrons moderated in the NE110 and then cap-

tured in the glass of the detector photomultiplier, and (4) delayed afterpulses from ion feedback in the photomultiplier. To eliminate some of the backgrounds and to facilitate corrections for the others, we recorded the flight-time spectra for the argon and for the compensator each in four separate time spectra corresponding to four contiguous bands of scintillator pulse heights. Thus, altogether we recorded eight spectra of 70 000 channels each. Henceforth, we denote the bands as bias 1 through bias 4. Legitimate neutron pulses arise from proton or carbon recoils from scattering in the scintillator. For a neutron energy E, the proton energies range from zero to E and the carbon energies from zero to $0.28E$. The pulse-height threshold for bias 1 corresponds to proton energies of only a few keV, and the thresholds for biases 2, 3, and 4 correspond to the maximum proton recoil energies produced by scattering of 0.05, 0.35, and 1.15 MeV neutrons. Since carbon ions have relatively small ionization efficiencies, their pulses are recorded in the lower biases. The γ-ray background pulses tend to be large because of the high ionization efficiencies for γ rays.

The use of bias groups allows us to eliminate completely the effects of some backgrounds from the calculated transmissions; the fact that the time spectrum of legitimate neutrons for a bias group extends only to the flight time corresponding to the bias threshold allows us to discard all backgrounds occurring subsequent to that cutoff, while still retaining later legitimate pulses in the lower biases. Furthermore, the bias groups allow us to prevent the recording of most of the afterpulses from ion feedback in the photomultiplier tube. We gate off the detector following any pulse in bias 4 and also any pulse produced by the initial γ-ray burst in biases 2 or 3. Thereby,

afterpulses from the most prolific sources are completely eliminated. Of course, this gating overrides the digital time analyzer deadtime (1.104 μsec) for the selected pulses. For argon and the compensator the resulting gating deadtime factors are 1.21 and 1.41, respectively, just after the γ-ray burst. These factors increase to 1.40 and 1.70, respectively, at the time of the bias 4 cutoff and remain constant thereafter. These deadtime factors have negligible uncertainty. Actually, all afterpulses could be eliminated by the simple requirement that the first event in any bias turn off the detector, but that procedure would cause large counting losses with little benefit from the further reduction in the number of afterpulses.

These deadtime-corrected data must then be corrected for the small backgrounds arising from the four sources listed above. We now describe the subtractions of these backgrounds in order of their increasing magnitudes.

Capture γ rays. The intensity of the 2.2-MeV γ rays from neutron capture in the source water moderator decays with a 17.5-μsec half-life. These γ rays create pulses in all four biases; they can be seen in bias 4 after 14 μsec because the neutron time spectrum extends only to 14 μsec. Our procedure is to determine the magnitude of the background in bias 4 and then to find the relative intensities in the lower three biases from a separate measurement with polyethylene placed in the neutron beam to remove most of the neutrons without seriously attenuating the γ rays. The corrections are small and have little uncertainty.

Boron γ rays. Because the glass envelope of the photomultiplier contains boron, the 478-keV γ rays from the ^{10}B$(n,\alpha\gamma)^7$Li reaction produce backgrounds in all bias groups. The bias-3 background is the largest and can be seen at flight times after 26 μsec. The observed background is almost time independent; we assume it is constant for flight times less than 26 μsec. To make corrections for the other bias groups we measure the relative backgrounds for the four groups by irradiating with a ^{7}Be source in a separate experiment.

Room background. We measure the time-independent background by including 1000 1-μsec channels at the late-time end of each spectrum because by such late times the time-dependent background counting rates are essentially zero. These corrections are also small and have little uncertainty.

Afterpulses. The largest and most complicated background is afterpulsing in the photomultiplier. We investigated the behavior of several RCA 8854 photomultipliers and found that an initial electron from the photocathode has a small but nonzero probability of producing a positive ion in the dynode structure; the ion can be accelerated back to the cathode where it produces a few electrons to create a small delayed pulse, i.e., an "afterpulse." The probability of ion production and the pulse-height and delay-time spectra of the afterpulses are characteristic of the particular photomultiplier and its operating conditions. Clearly, the probability that an initial event will produce an afterpulse is proportional to the number of photoelectrons or to the pulse height for the event. That is the reason for our use of the gating described above to prevent the recording of afterpulses from large initial pulses.

Since the gating is only for large initial pulses, there remains a background generated by initial proton recoils in the lower bias groups. Since the afterpulses in a given time channel are produced by a broad time spectrum of earlier neutrons, the effect is to introduce an erroneous cross-section component which is an average for higher-energy neutrons. This is most serious when the later channel corresponds to a neutron resonance energy, where the correct cross section is much larger than the earlier average. Thus, the effect can be seen from a comparison of the transmission minima for bias 1 and bias 2, where the afterpulses occur, to bias 3 and bias 4, which are free of afterpulses; the observed minima are not deep enough for bias 1 and bias 2.

The following corrections for the afterpulses are based on reasonable approximations with the choice of one empirical constant. Our studies of RCA 8854 phototubes show that most afterpulses occur within 1 or 2 μsec after the original pulse, but a few can occur as much as 25 μsec later. The clock deadtime prevents the recording of those within the first 1.1 μsec. The time spectrum is complicated. We make the good approximation that 75% of the recorded afterpulses are distributed uniformly in the 1-μsec interval from 1.1 to 2.1 μsec after the initial pulse and the remaining 25% are distributed uniformly in the 8-μsec interval from 2.1 to 10.1 μsec. For a bias group b, the number of afterpulses is proportional to the average proton recoil energy E_b. The number of afterpulses per time interval at a flight time T μsec is then

$$AP(T) = \sum_{b=1}^{3} C \left[\frac{1}{4} \frac{\int_{T-10.1}^{T-2.1} dt\, E_b(t) N_b(t)}{\int_{T-10.1}^{T-2.1} dt} + \frac{3}{4} \frac{\int_{T-2.1}^{T-1.1} dt\, E_b(t) N_b(t)}{\int_{T-2.1}^{T-1.1} dt} \right], \qquad (2.5)$$

where C is a parameter to be adjusted, as discussed below. The summation is only over the lower three bias groups that are allowed to give afterpulses. The integrals are evaluated numerically; the quantity $N_b(t)dt$ is the deadtime-corrected counts for a channel of width dt at flight time t. The γ-ray burst is excluded from the integrals for bias 2 and bias 3 because of the gating. For each bias group the average energy $E_b(t)$ is a function of t. For early flight times, which correspond to high-energy neutrons, the bias groups are "filled" with pulses such that the average energies are constants corresponding to the centers of the groups, namely, 0.025, 0.2, and 0.75 MeV for $b=1$, 2, and 3. At later times $E_b(t)$ decreases as the maximum recoil pulses decrease toward the lower threshold of the group.

The coefficient C is a constant characteristic of the photomultiplier and its operating conditions. Our studies of other RCA 8854 tubes showed that C is approximately 0.05 MeV^{-1}. However, since we did not study the afterpulsing characteristics of the particular photomultiplier used in this transmission measurement, we estimate C subject to two experimental criteria. First, we recognize that all afterpulses occur in bias 1 or bias 2, and we adjust C to give consistency to the transmission minimum found

in these two groups with those in the two higher bias groups. For this purpose we distribute the calculated afterpulses in the ratio of 2/1 for bias 1/bias 2. This ratio is based on the observed afterpulses that are produced by the γ-ray burst and found in bias 1 and bias 2 at about 1.2 μsec after the burst, i.e., just after the clock deadtime. Secondly, we require at low energies that the final cross sections agree well with the predictions at the peaks of the well-resolved s-wave resonances. As reviewed in the next section, the peak cross section for a broad s-wave resonance is the sum of the cross section observed at the interference minimum plus $4\pi/k^2$, where k is the neutron wave number at the peak. In particular, we require good agreement at the 173-keV resonance, which has a transmission minimum of only 4% and so provides a good standard for the background subtraction. Thus we find

$$C = 0.06 \text{ MeV}^{-1} , \qquad (2.6)$$

which agrees well with our measurements on similar photomultiplier tubes under similar operating conditions.

Only small uncertainties propagate from the background corrections to the cross sections. For example, at the minimum of the 173-resonance, there are about 150 deadtime-corrected counts/nsec observed and the backgrounds are 0.3, 1.4, 4.2, and 16.5 counts/nsec, respectively, for the n-p capture, boron, room, and afterpulse components. Thus, even at this deep minimum the sum of backgrounds is only 15% of total observed counts. At 77 keV there is an s-wave resonance for which the predicted transmission minimum is only 0.05%. Here the observed counts are nearly all from backgrounds. Our deduced backgrounds in the transmission minimum for this resonance are 0.13, 1.4, 4.2, and 0.8 counts/nsec for n-γ, boron, room, and afterpulsing, respectively. Only one additional count/nsec of background must be assumed to force agreement with the known cross section at the peak. We see that the deduced backgrounds are small and are known with little uncertainty.

At high neutron energies, $E > 29$ MeV, we make a more drastic correction for afterpulsing. A peak of afterpulses is clearly observed in bias 1 and bias 2, just following the 1.014-μsec deadtime from the γ-ray burst, and the number of afterpulses in the peak is greater than the neutron counts. Thus, a reliable correction cannot begin until about 2.0 μsec after the burst. For this reason we use only the counts observed in bias 3 and bias 4 for the first 2.6 μsec after the γ-ray burst, i.e., for $E > 29$ MeV.

III. EXPERIMENTAL RESULTS

The transmission $T(E)$ observed for a time channel corresponding to the neutron energy E is

$$T(E) = \frac{M_{\text{com}}(E)C_{\text{Ar}}(E)}{M_{\text{Ar}}(E)C_{\text{com}}(E)} , \qquad (3.1)$$

where $C_{\text{Ar}}(E)$ and $C_{\text{com}}(E)$ are the counts for the argon sample and for the compensator, corrected for deadtime and background, and where M_{Ar} and M_{com} are the corresponding neutron monitor counts. The observed total

cross section is

$$\sigma_T(E) = -\frac{1}{n}\ln[T(E)] , \qquad (3.2)$$

where n is the sample thickness, i.e., 0.211 atom/b.

The symbols in Figs. 2–4 represent $\sigma_T(E)$ for $E < 1.6$ MeV, i.e., for energies extending slightly above the region where the energy resolution and the multilevel structure allow an R-matrix analysis. The statistical uncertainties are less than the symbol heights. The points plotted over the very narrow resonances represent the observed cross section, but the points in regions where the cross section varies more slowly represent energy averages of the original data. The averaged points facilitate the R-matrix analysis and improve the visual presentation in the data. The smooth curves represent the R-matrix parametrization to be described in Secs. IV and V.

For $1.0 < E < 50$ MeV the histogram in Fig. 5 represents the average $\langle \sigma_T(E) \rangle$ obtained by averaging over energy intervals selected to yield a relatively smooth plot. The fluctuations are due to the statistical counting uncertainties. We note that, for energies up to a few
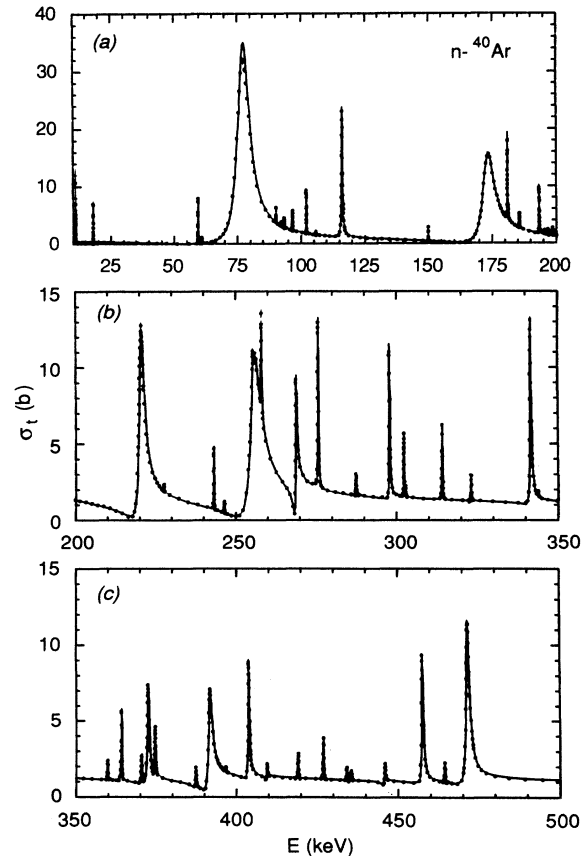
FIG. 2. Total cross section for $n + {}^{40}\text{Ar}$. The points represent the measured cross section over the interval 10 to 500 keV. Between resonances the cross sections have been averaged in order to facilitate analysis of the data. The curve represents the multilevel R-matrix description using the parameters in Tables I–III and the boundary radius $a_c = 5.0$ fm.
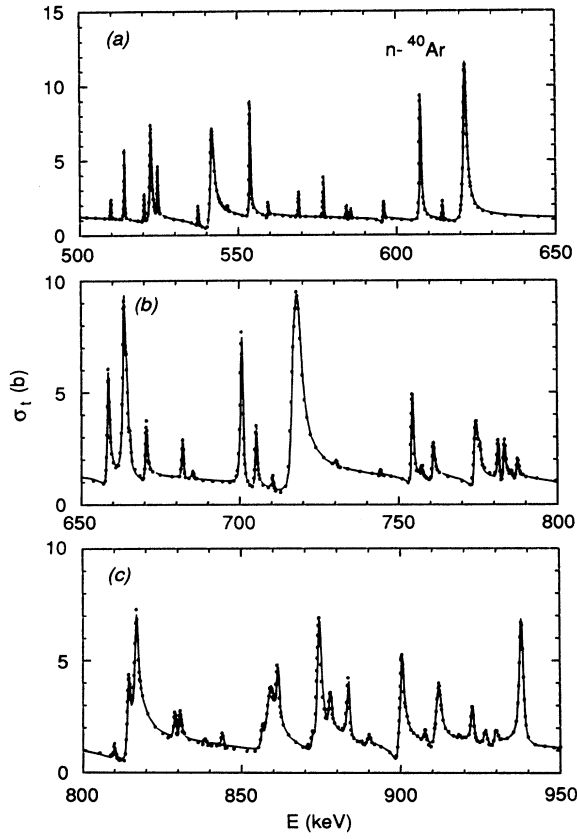
FIG. 3. Similar to Fig. 2 except for the energy interval.
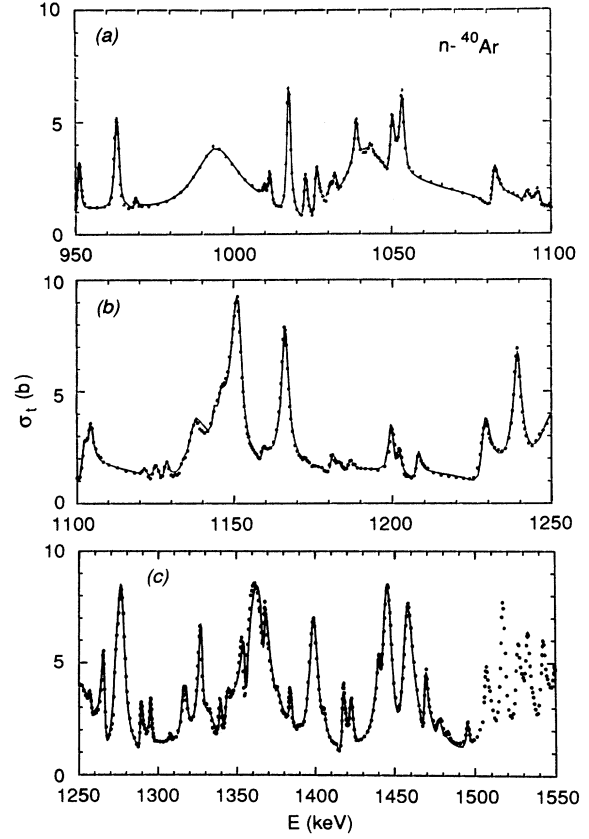
FIG. 4. Similar to Fig. 2 except for the energy interval.

MeV, the averages presented in Fig. 5 are more accurate than could be obtained from measurements[14] of average transmissions in an experiment with poor energy resolution. In such measurements one must assume that the average quantities, $\langle T(E)\rangle$ and $\langle \sigma_T(E)\rangle$, are related in the same manner as are $T(E)$ and $\sigma_T(E)$ in Eq. (3.2). However, that assumption is invalid if $\sigma_T(E)$ varies rapidly within the averaging interval.

IV. R-MATRIX FORMALISM

For the present case of a spin-0 nuclide with negligible absorption and for neutron energies below the inelastic threshold, $E < 1.50$ MeV, the scattering function $S_{lJ}(E)$ for neutron orbital and total angular momentum l and J can be expressed in terms of a real phase shift, $\delta_{lJ}(E)$:

$$S_{lJ}(E) = e^{2i\delta_{lJ}(E)} ,\qquad (4.1)$$

and the total cross section is a function of the phase shift,

$$\sigma_{lJT}(E) = \frac{4\pi}{k^2} g(J)\sin^2\delta_{lJ}(E) ,\qquad (4.2)$$

where $g(J)$ is the statistical spin factor and k is the neutron wave number. To fit the data we parametrize the phase shifts using the R-matrix formalism[15]

$$\delta_{lJ}(E) = \phi_l(E) + \tan^{-1}[P_l(E)R_{lJ}(E)] ,\qquad (4.3)$$

where P_l and ϕ_l are, respectively, the l-wave penetrability and hard-sphere phase shift evaluated at the channel radius, for which we use

$$a_c = 1.45 A^{1/3} .\qquad (4.4)$$

In writing Eq. (4.3) we have set the boundary conditions equal to the shift factors at all energies.

The R function $R_{lJ}(E)$ is a sum over all the resonances with quantum numbers lJ observed within the region or domain of the analysis, plus a smoothly increasing function of energy which describes the aggregate effect of levels external to the domain,

$$R_{lJ}(E) = \sum_{\lambda=1}^{N} \frac{\gamma_{lJ\lambda}^2}{E_{lJ\lambda}-E} + R_{lJ}^{\text{ext}}(E) ,\qquad (4.5)$$

where $\gamma_{lJ\gamma}^2$ and $E_{lJ\lambda}$ are free parameters representing the reduced width and energy of the λth resonance with angular momenta l and J.

In order to evaluate the external R function $R_{lJ}^{\text{ext}}(E)$ we first note that if the actual discrete levels for all energies are replaced by a continuous density of reduced widths, i.e., a strength function $s_{lJ}(E)$, then a smoothed real R function can be defined[15−18]

$$\overline{R}_{lJ}(E) = P \int_{-\infty}^{+\infty} \frac{s_{lJ}(E')dE'}{E'-E} ,\qquad (4.6)$$
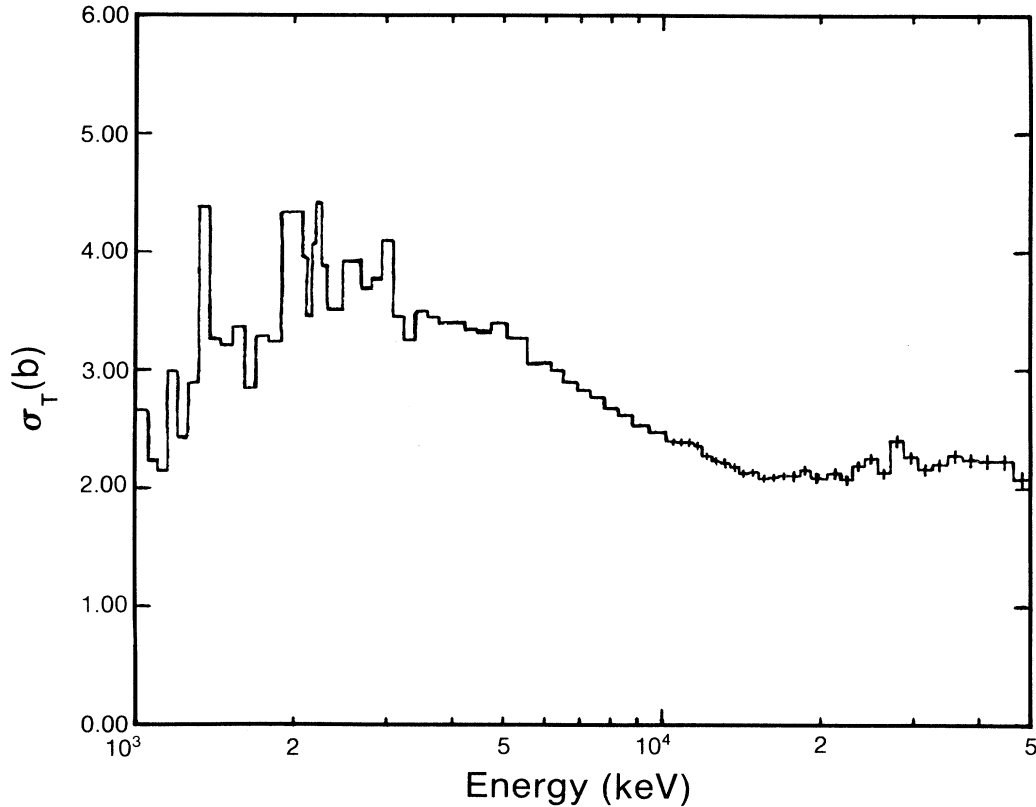
FIG. 5. Average cross section for $n + {}^{40}\mathrm{Ar}$ from 1 to 50 MeV. The cross sections have been averaged over suitable energy intervals in order to produce a relatively smooth plot. The error bars represent the uncertainties due to counting statistics.

where P denotes the principal value integral. The external R function is found by subtracting the contribution from levels within the domain $[E_1 = 0.007$ MeV, $E_2 = 1.521$ MeV],

$$R_{IJ}^{\mathrm{ext}}(E) = \overline{R}_{IJ}(E) - P \int_{E_1}^{E_2} \frac{s_{IJ}(E')dE'}{E' - E} . \tag{4.7}$$

If the strength function is chosen consistently with the observed strength within the domain, this formulation can give a good average description of the effects of the external levels, especially near the end points where the effects of levels just outside the domain are particularly important.

We parametrize $s_{IJ}(E)$ and $\overline{R}_{IJ}(E)$ by

$$s_{IJ}(E) = \alpha_{IJ} + \beta_{IJ}(E - E_1) \tag{4.8}$$

and

$$\overline{R}_{IJ}(E) = a_{IJ} + b_{IJ}(E - E_1) , \tag{4.9}$$

where the coefficients are free parameters. The choice of $s_{IJ}(E)$ follows an iterative procedure; it is finally chosen to give a good description of the observed average reduced neutron width per energy interval, $\langle \gamma_{IJ\lambda}^2 \rangle / D_{IJ}$, within the domain $[E_1, E_2]$.

V. DETERMINATION OF MULTILEVEL PARAMETERS

Given the excellent energy resolution of ORELA, the detailed energy dependence of the $n + {}^{40}\mathrm{Ar}$ cross section can be used to determine the $s_{1/2}$, $p_{1/2}$, $p_{3/2}$, $d_{3/2}$, and $d_{5/2}$ R-matrix parameters and, thereby, to deduce the functions for those partial waves. Because the d-wave J assignments are difficult to make, these scattering functions are less well determined than are the s- and p-wave scattering functions.

The adjustment of the R-matrix parameters was done using an interactive computer program[19] which calculates the cross section for a set of estimates for the R-matrix resonance parameters: the resonance energies E_λ, the reduced neutron widths γ_λ^2, the orbital and total angular momentum quantum numbers (l,J), and the external R functions R_{IJ}^{ext}.

The interactive program[19] produces a plot of both the calculated and measured cross sections for comparison. The user interactively modifies any of the input parameters and immediately sees the effect of the change. In particular, the use of the program greatly facilitates making the (l,J) assignments. In making these assignments we use the fact that resonances with the same (l,J) interfere producing a distinctive pattern. Such a pattern is clearly visible in Fig. 4 near 1 MeV where three wide s-

wave resonances interfere. In fact, as seen in Fig. 4, there is a series of wide interfering resonances continuing from ≈ 1 to 1.5 MeV. These wide overlapping resonances must all be of the same (l,J). We make the assumption that these are s-wave resonances. A $p_{1/2}$ assignment for these wide resonances produces an unrealistically large $p_{1/2}$ strength function.

Having determined the resonance energies, the (l,J) assignments, and the R_{lJ}^{ext} parameters, and also having established good estimates for the neutron widths, we made final small adjustments to the widths by solving Bayes' equations using the computer program SAMMY.[20,21] In addition to the resonance parameters E_λ, l, J, $g_J\gamma_\lambda^2$, and $g_J\Gamma_\lambda$, the program SAMMY includes the radiation widths Γ_γ. However, for energies above a few keV the shapes are dominated either by the resolution of the measurement or by the much larger neutron widths, and the resonance shapes are insensitive to the Γ_γ. Thus we approximate the Γ_γ by using values[22] typical for this mass region, i.e., the Γ_γ are held fixed at 1000 meV for all even-parity resonances and 500 meV for those of odd parity. The use of SAMMY also yields estimates of the uncertainties and correlations among the parameters. The final R-matrix parameters are given in Tables I, II, and III. In Table I are listed the resonance parameters E_λ, l, J,

$g_J\gamma_{lJ\lambda}^2$, and $g_J\Gamma_\lambda$. Blank spaces are used in Table I to indicate those l and/or J assignments which are uncertain. We list the products with g_J because only the products are determined in those cases for which the J^π assignments are uncertain. The quantities Γ_λ listed in Table I are calculated from the reduced neutron widths by

$$\Gamma_\lambda = 2P_l\gamma_\lambda^2 , \qquad (5.1)$$

where the P_l are the neutron penetrabilities and the Γ_λ are often referred to as the "observed" widths of the resonances. Actually these widths can differ considerably from the observed width of a peak in the cross section because of interference with nearby resonances with the same (l,J). Another consequence of multilevel interference is that the peak position may differ from E_λ, even though the boundary condition has been set equal to the energy shift factor. Both Γ_λ and the peak position depend on the assumed boundary radius. Even so, the scattering functions are well determined and are not functions of the boundary conditions.

In Tables II and III are listed the parameters comprising the functions s_{lJ} and $\overline{R}_{lJ}$ required in the calculation of the external R functions. Using the parameters in Tables I–III, the total cross sections for 0.015 to 1.5 MeV are calculated and shown in Figs. 2, 3, and 4 as solid curves.

TABLE I. R-matrix resonance parameters for $n + {}^{40}\text{Ar}$ for the neutron energy range 10–1500 keV.

E (keV)[a]	J^{π}[b]	$g\Gamma_n$ (eV)	γ_λ^2 (eV)	E (keV)[a]	J^{π}[b]	$g\Gamma_n$ (eV)	γ_λ^2 (eV)
11.181		0.18±0.01		387.394		50±2	
17.974		0.46±0.02		387.812		10±1	
59.309	$\frac{1}{2}^-$	6.36±0.12	191	391.347	$\frac{1}{2}^+$	1290±5	965
60.917		0.69±0.04		396.701		12±2	
76.486	$\frac{1}{2}^+$	5672±3	9 573	403.785	$\frac{3}{2}^-$	537±3	1 245
90.057		3.98±0.16		409.382	$\frac{1}{2}^+$	36±2	27
92.075		1.0±0.1		419.152		94±3	
93.276		2.0±0.1		426.942		182±3	
96.538		5.4±0.2		434.124		40±2	
101.986		27.9±0.6		435.550		26±2	
105.693		1.1±0.1		445.800	$\frac{1}{2}^+$	67±2	47
116.051	$\frac{1}{2}^-$	435±1	5 068	457.528	$\frac{3}{2}^-$	880±4	1 764
149.885	$\frac{3}{2}^-$	12.0±0.4	99	464.459		87±3	
172.267	$\frac{1}{2}^+$	5550±6	6 240	471.551	$\frac{3}{2}^-$	2270±7	4 393
180.974	$\frac{3}{2}^-$	205±2	1 309	517.127	$\frac{1}{2}^+$	144±3	94
185.570		24.3±0.8		518.112		77±3	
193.324	$\frac{3}{2}^-$	106±1	621	533.811	$\frac{5}{2}^-$	1114±5	
195.412		5.8±0.4		538.647		15±2	
196.694		7.1±0.4		554.022	$\frac{3}{2}^-$	507±4	818
198.550		9.8±0.5		561.617		63±3	
220.127	$\frac{1}{2}^+$	1920±4	1 910	571.172	$\frac{3}{2}^-$	4856±1	7 573
227.630		3.4±0.3		576.469		30±3	
243.197	$\frac{3}{2}^+$	74±1	8 934	581.269		20±2	
246.488		9.0±0.5		593.541	$\frac{1}{2}^-$	1272±9	1 902
255.079	$\frac{1}{2}^+$	3785±6	3 497	596.615	$\frac{1}{2}^+$	4973±2	3 005
255.425		26.0±1.6		606.422	$\frac{3}{2}^-$	662±5	966
258.126	$\frac{3}{2}^-$	158.4±2.5	634	607.760		59±4	
268.716	$\frac{1}{2}^+$	398±2	359	624.506	$\frac{3}{2}^+$	475±5	6 362

TABLE I. (Continued).

E (keV)[a]	J^{π}[b]	$g\Gamma_n$ (eV)	γ_{λ}^2 (eV)	E (keV)[a]	J^{π}[b]	$g\Gamma_n$ (eV)	γ_{λ}^2 (eV)
275.764	$\frac{3}{2}^+$	332±2	29 602	630.282	$\frac{1}{2}^-$	1255±1	1 757
287.454		29±2		631.065	$\frac{5}{2}^-$	1820±1	
297.869	$\frac{3}{2}^-$	368±2	1 235	658.551	$\frac{3}{2}^-$	968±7	1 294
302.314		142±2		663.670	$\frac{5}{2}^+$	1765±1	20 674
302.709		13±1		664.570	$\frac{3}{2}^\pm$	683±1	7 976
314.181	$\frac{3}{2}^+$	157±2	10 267	665.278	$\frac{1}{2}^+$	273±6	156
323.110		52±2		670.547	$\frac{3}{2}^-$	400±5	524
341.628	$\frac{3}{2}^-$	770±3	2 182	682.113	$\frac{3}{2}^+$	271±4	2 993
343.858		9±1		685.421		43±1	
359.915		50±2		700.749	$\frac{5}{2}^-$	1704±8	
364.204	$\frac{3}{2}^+$	216±2	9 958	705.193	$\frac{3}{2}^-$	497±5	618
370.428		85±2		710.460		107±5	
372.468	$\frac{1}{2}^-$	620±3	1 583	716.624	$\frac{1}{2}^-$	2052±2	2 506
374.595	$\frac{3}{2}^-$	137±2	347	718.125	$\frac{3}{2}^-$	4881±2	5 950
730.479		29±3		962.889	$\frac{5}{2}^+$	1394±40	7 345
744.497		20±2		963.796		812±38	
754.372	$\frac{5}{2}^-$	481±43		969.147		108±7	
754.526	$\frac{3}{2}^-$	422±13	488	983.350	$\frac{1}{2}^+$	39 273±123	18 483
757.550		86±5		1010.348		154±15	
760.998	$\frac{1}{2}^-$	366±6	420	1011.803	$\frac{5}{2}^+$	533±13	2 536
773.827	$\frac{1}{2}^+$	1674±18	8 888	1016.709	$\frac{1}{2}^-$	980±18	842
775.871		100±6		1017.845	$\frac{5}{2}^+$	1896±20	8 912
781.428	$\frac{3}{2}^+$	380±6	3 113	1022.650	$\frac{3}{2}^-$	758±13	648
783.267	$\frac{3}{2}^-$	380±6	424	1026.162	$\frac{3}{2}^-$	890±19	758
785.405	$\frac{1}{2}^+$	46±4	24	1030.278	$\frac{1}{2}^-$	288±13	245
787.331	$\frac{1}{2}^-$	157±6	174	1032.190	$\frac{5}{2}^+$	294±12	1 344
810.012		121±6		1033.592	$\frac{1}{2}^+$	21 387±95	9 818
814.285	$\frac{3}{2}^-$	802±13	859	1039.054	$\frac{5}{2}^+$	782±16	3 525
816.723	$\frac{1}{2}^-$	4162±26	4 442	1043.007	$\frac{1}{2}^-$	186±15	156
817.112	$\frac{5}{2}^-$	789±9		1049.969	$\frac{3}{2}^-$	1256±18	1 046
829.162		378±8		1053.526	$\frac{5}{2}^+$	1829±19	8 013
830.535	$\frac{3}{2}^-$	321±6	337	1081.578	$\frac{1}{2}^+$	1589±27	713
838.655		46±4		1092.214	$\frac{1}{2}^+$	243±14	108
844.003		138±6		1095.842	$\frac{5}{2}^+$	208±10	842
856.551		210±8		1101.672	$\frac{1}{2}^+$	2901±53	1 290
857.318	$\frac{1}{2}^+$	6132±46	3 091	1104.149	$\frac{3}{2}^-$	688±22	546
861.192	$\frac{3}{2}^-$	616±11	623	1121.560		78±7	
871.090		86±3		1125.176		237±12	
872.332		278±8		1128.537		358±12	
874.115	$\frac{3}{2}^-$	2861±19	2 851	1133.113		47±4	
874.625	$\frac{3}{2}^+$	272±12	1 752	1133.193	$\frac{1}{2}^+$	13 374±139	5 863
877.695	$\frac{1}{2}^-$	489±10	485	1145.024	$\frac{1}{2}^-$	5434±77	4 173
883.569	$\frac{3}{2}^+$	755±9	4 766	1151.163	$\frac{5}{2}^+$	9568±54	35 062
889.842	$\frac{1}{2}^-$	98±6	96	1159.250	$\frac{3}{2}^-$	250±12	190
899.120	$\frac{1}{2}^+$	48±5	24	1166.175	$\frac{5}{2}^+$	6901±35	24 645
900.181	$\frac{3}{2}^-$	2032±14	1 967	1172.919		39±4	
907.861		159±8		1180.568	$\frac{3}{2}^-$	342±13	255
911.510	$\frac{1}{2}^-$	1218±18	1 165	1183.585		76±7	
912.329	$\frac{3}{2}^+$	179±9	1 054	1186.221	$\frac{1}{2}^-$	159±10	118
918.552	$\frac{5}{2}^-$	27±3		1199.833	$\frac{3}{2}^+$	1261±19	4 256
922.624	$\frac{5}{2}^+$	500±9	2 881	1202.191		463±14	
926.658	$\frac{3}{2}^+$	144±7	820	1207.698	$\frac{1}{2}^+$	1577±47	670
929.693	$\frac{3}{2}^-$	169±7	159	1228.221	$\frac{1}{2}^-$	4090±57	2 944

TABLE I. (Continued).

E (keV)[a]	J^{π}[b]	$g\Gamma_n$ (eV)	γ_λ^2 (eV)	E (keV)[a]	J^{π}[b]	$g\Gamma_n$ (eV)	γ_λ^2 (eV)
938.031	$\frac{5}{2}^+$	2778±14	15 458	1229.426		348±16	
950.830	$\frac{1}{2}^-$	217±13	199	1239.303	$\frac{5}{2}^-$	5678±37	
951.575		555±16		1243.182	$\frac{1}{2}^+$	26 577±230	11 124
1245.642		141±13		1376.620		395±23	
1257.454	$\frac{5}{2}^+$	500±21	1 541	1384.254		1410±29	
1265.840	$\frac{5}{2}^+$	3504±34	10 651	1398.962	$\frac{5}{2}^+$	16 237±76	40 736
1272.844	$\frac{1}{2}^-$	2090±49	1 456	1405.671		579±23	
1276.692	$\frac{5}{2}^+$	16 777±80	50 155	1417.177	$\frac{3}{2}^-$	1419±48	898
1288.773	$\frac{3}{2}^-$	1321±22	910	1418.269	$\frac{5}{2}^+$	1272±45	3 109
1295.272	$\frac{3}{2}^+$	1068±22	3 106	1422.937	$\frac{5}{2}^+$	1842±33	4 475
1307.287		150±15		1434.032	$\frac{1}{2}^+$	53 041±366	20 671
1312.293	$\frac{1}{2}^+$	25 484±336	10 382	1440.978	$\frac{5}{2}^+$	2639±59	6 263
1325.976	$\frac{1}{2}^+$	15 109±173	6 123	1445.206	$\frac{5}{2}^+$	18 925±115	44 662
1327.007	$\frac{5}{2}^+$	7129±66	19 780	1458.353	$\frac{5}{2}^+$	22 043±125	51 146
1328.543		49±5		1469.110	$\frac{5}{2}^+$	3142±46	7 191
1333.760		155±14		1478.416		660±25	
1338.759	$\frac{3}{2}^-$	1207±29	804	1482.779		228±18	
1343.386	$\frac{3}{2}^-$	1115±29	740	1494.673	$\frac{1}{2}^+$	107 900±795	41 189
1354.209	$\frac{5}{2}^+$	5513±72	14 714	1495.134		773±25	
1354.588	$\frac{1}{2}^+$	39 767±263	15 946	1507.321	$\frac{5}{2}^+$	3716±318	8 110
1361.339	$\frac{5}{2}^+$	37 374±155	98 750	1509.000		800±80	
1367.616	$\frac{5}{2}^+$	2814±57	7 369	1517.950	$\frac{5}{2}^+$	28 899±972	62 247

[a]The uncertainty in the resonance energy is one resolution width as calculated using Eq. (2.2).
[b]Blank spaces indicate that the J^{π} could not be unambiguously determined.

Comparison with earlier work

Liou et al.[7] and Siebel[8] report six s-wave resonances below 400 keV (see Table IV). Seibel reports an additional s-wave resonance at 596 keV. As shown in Table IV, these results are in excellent agreement with the energies and widths from the present much higher resolution work. We identify three additional narrow s-wave resonances between 400 and 590 keV. Of course, the present measurement extends well beyond the energy range of the earlier work and we identify 18 additional s-wave resonances between 600 and 1500 keV.

The p-wave assignments are more difficult because the

TABLE II. Average parameters for $n + {}^{40}$Ar.

$J\pi$	N_{lJ}^{obs}	N_{lJ}^{m}	D_{lJ}^{a} (keV)	Δ_3^{obs}	$\Delta_3^{\text{expected}}$
$\frac{1}{2}^+$	28	2	49±5	0.26[b]	0.29±0.11
$\frac{1}{2}^-$	20	5	51±5	0.33	0.29±0.11
$\frac{3}{2}^-$	34	14	26±2	0.33	0.29±0.11
$l = 2$	47[c]		31±3		

[a]Corrected for missing resonances.
[b]Δ_3^{obs} calculated over energy interval [0.0,1100 keV] for $s_{1/2}$, [0 to 750 keV] for $p_{1/2}$, and [175 to 800 keV] for $p_{3/2}$.
[c]Not corrected for missing resonances.

p-wave resonance widths are much narrower than are the s-wave resonances. Even so, we are able to make (l,J) assignments for 20 $p_{1/2}$ and for 34 $p_{3/2}$ resonances. In Table V a comparison with the earlier work[7,8] is given. The agreement with the earlier work is, with only a few exceptions, excellent. We cannot make (l,J) assignments for the first two narrow resonances observed in our measurement since the total width of each of these resonances is very much smaller than the resolution width of the measurement. Liou et al.[7] made the p-wave assignments based on the lack of observable asymmetry, but the shape of very narrow s-wave resonances would be dominated by the resolution function, masking any asymmetry. Hence there appears no evidence to support the p-wave assignment for these two resonances. The three p-wave assignments for which Liou et al.[7] were able to make J assignments agree with our assignments. We disagree with their p-wave assignment for the 275- and 533.8-keV resonances and are able to identify three p-wave resonances between 10 and 600 keV not reported in the earlier work. Above 450 keV, some of the neutron widths reported by Liou et al.[7] are significantly smaller than those from the present work, perhaps because the area analysis performed for the p-wave resonances by Liou et al. depends critically on establishing the shape of the cross section on either side of a resonance. We identify 39 additional p-wave resonances between 600 and 1500 keV.

TABLE III. Parameters for the smooth R functions, $\bar{R}_{lJ}$, and the strength functions, s_{lJ}.

| $J\pi$ | $\bar{R}_{lJ}$ | | $\Delta\bar{R}_{lJ}$ | s_{lJ}[b] | |
	a	b (eV^{-1})		α	β (eV^{-1})
$\frac{1}{2}^{+}$	0.51	7.9×10^{-8}	0.04[a]	0.018±0.008	$(5.7\pm1.7)\times10^{-8}$
$\frac{1}{2}^{-}$	-0.37	0.16×10^{-8}	0.04	0.024±0.008	
$\frac{3}{2}^{-}$	-0.18	4.4×10^{-8}	0.03	0.019±0.004	
$\frac{3}{2}^{+}$	0.10		0.02	0.045±0.017	
$\frac{5}{2}^{+}$	0.35		0.05	0.19±0.05	
$l=2$				0.47±0.10	

[a]Uncertainty in $\bar{R}_{lJ}$ at midpoint of $[E_1,E_2]$.
[b]$a_c=5.0$ fm.

TABLE IV. A comparison with earlier work for s-wave resonances between 10 and 600 keV.

| E_λ (keV) | | | Γ_n (keV) | | |
Present work	Liou et al.[7]	Siebel[8]	Present work	Liou et al.	Siebel[8]
76.436	76.2±0.4	77	5.6±0.5	5.5±0.4	4
172.246	171.7±0.5	173	5.5±0.6	4.5±0.4	4.2
220.120	219.4±0.5	221	1.9±0.2	1.8±0.2	2.0
255.068	254.3±0.5	255	3.8±0.4	3.4±0.4	3.3
268.714	267.6±0.5	268	0.40±0.04	0.52±0.12	0.25
391.339	390.6±0.9	388	1.31±0.13	1.4±0.3	0.9
409.378			0.038±0.004		
445.800			0.07±0.007		
517.120			0.15±0.01		
593.559		596	5.1±0.5		4

TABLE V. A comparison with earlier work for non-s-wave resonances between 10 and 600 keV.

| E_λ (keV) | | | J^π | | Γn (keV) | | |
a	b	c	a	b	a	b	c
11.181	11.17			$(\frac{1}{2},\frac{3}{2})^{-}$	0.17±0.02	0.14±0.03	
17.974	17.95			$(\frac{1}{2},\frac{3}{2})^{-}$	0.46±0.05	0.42±0.07	
59.309	59.25		$\frac{1}{2}^{-}$	$(\frac{1}{2},\frac{3}{2})^{-}$	6.4±0.6	5.9±0.8	
116.051	115.7	116	$\frac{1}{2}^{-}$	$\frac{1}{2}^{-}$	430±43	390±50	500
180.975	180.4	181	$\frac{3}{2}^{-}$	$(\frac{1}{2},\frac{3}{2})^{-}$	203±20	220±50	300
193.325	192.8		$\frac{3}{2}^{-}$	$(\frac{1}{2},\frac{3}{2})^{-}$	105±10	90±25	
258.127			$\frac{3}{2}^{-}$		158±16		
275.766	274.7	275	$\frac{3}{2}^{+}$	$(\frac{1}{2},\frac{3}{2})^{-}$	329±33	260±80	250
297.871	296.9	297	$\frac{3}{2}^{-}$	$(\frac{1}{2},\frac{3}{2})^{-}$	366±37	300±90	300
	301.1	302		$(\frac{1}{2},\frac{3}{2})^{-}$		150±50	100
341.632	340.8	338	$\frac{3}{2}^{-}$	$\frac{3}{2}^{-}$	770±77	720±100	500
372.473	371.3		$\frac{1}{2}^{-}$	$(\frac{1}{2},\frac{3}{2})^{-}$	623±62	740±160	
374.598			$\frac{3}{2}^{-}$		139±1		
403.789	401.7		$\frac{3}{2}^{-}$	$(\frac{1}{2},\frac{3}{2})^{-}$	539±54	410±120	
457.534	455.4		$\frac{3}{2}^{-}$	$(\frac{1}{2},\frac{3}{2})^{-}$	888±89	530±140	
471.563	469.3		$\frac{3}{2}^{-}$	$\frac{3}{2}^{-}$	2299±230	1700±400	
533.816	531.6		$\frac{5}{2}^{+}$	$(\frac{1}{2},\frac{3}{2})^{-}$	1126±127	520±150	
554.031	552.8		$\frac{3}{2}^{-}$	$(\frac{1}{2},\frac{3}{2})^{-}$	515±51	300±90	
571.197	569.3		$\frac{3}{2}^{-}$	$(\frac{1}{2},\frac{3}{2})^{-}$	4927±493	2700±800	
593.559			$\frac{1}{2}^{-}$		1301±130		

[a]Present work.
[b]Liou et al. (Ref. 7).
[c]Siebel (Ref. 8). No J^π assignments for non-s-wave resonances are made by Siebel.

VI. AVERAGE PROPERTIES

The average properties of interest from the R-matrix analysis are the mean level spacings D_{lJ}, the level densities $\rho_J(E)$, the strength functions s_{lJ}, and the R_{lJ}^{ext} functions. These are the quantities which can easily be compared with results from statistical and optical model calculations.

A. Average resonance spacings

Since the resonance spacing in $n + {}^{40}\text{Ar}$ is large, we expect to miss relatively few s- and p-wave resonances. In order to estimate the number of missed resonances of given (l,J) over our measurements range, we assume that the observed reduced widths are drawn from a Porter-Thomas (PT) distribution[23] and that no resonances are missed with reduced widths, γ_λ^2, greater than $\langle \gamma_\lambda^2 \rangle /4$, where the angle-bracket notation indicates the result of

averaging. In order to perform this test,[24] we form a subset of resonances with given (l,J), beginning with the largest reduced width and including successively smaller widths until the ratio $\gamma_\lambda^2 / \langle \gamma_\lambda^2 \rangle$ is the result expected for a sample obtained by drawing widths larger than $\frac{1}{4}$ the distribution mean reduced width from a PT distribution. The observed average reduced width for the resonances included in the subset provides a measure of the population mean and therefore provides a correction for missing resonances. The results of this test for $s_{1/2}$, $p_{1/2}$, and $p_{3/2}$ resonances are shown in Fig. 6 where the histograms are the observed distributions and the solid curves are from the PT distributions which best describe the data. Extrapolation of the solid curves to zero reduced width yields the number of missed resonances, $N^m = 2$, 5, and 14, for $s_{1/2}$, $p_{1/2}$, and $p_{3/2}$ resonances, respectively. The dashed curves in Fig. 6 are the expected distributions assuming no missed resonances.

Given the small penetrabilities for d-wave resonances, we expect to be able to identify only the resonances with rather large neutron widths, at least in the lower part of the experimental energy range. In fact the first $d_{3/2}$ resonance is identified at 240 keV and the first $d_{5/2}$ resonance
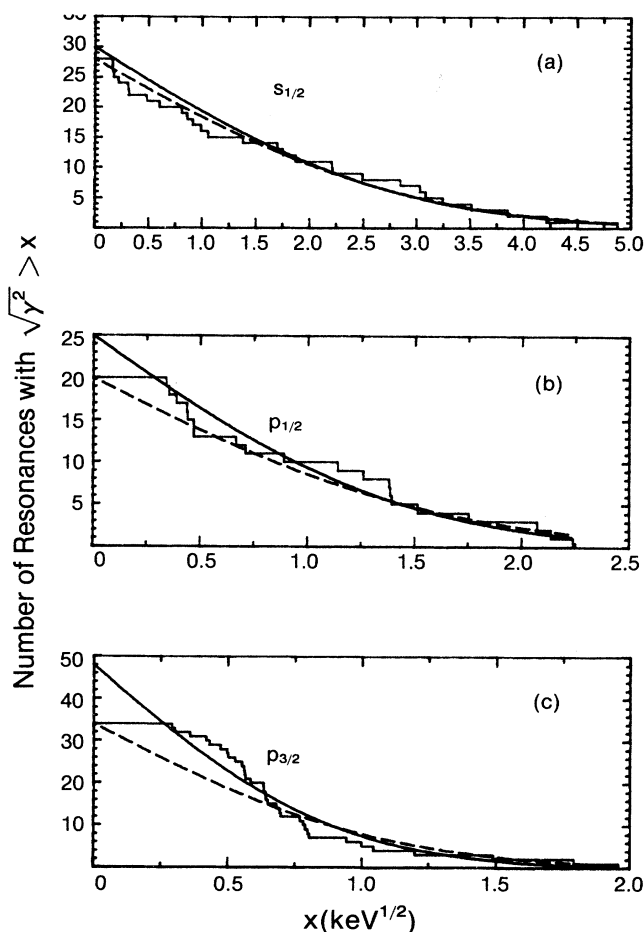
FIG. 6. Porter-Thomas test for missing resonances. The histograms represent the number of $s_{1/2}$, $p_{1/2}$, and $p_{3/2}$ resonances with $(\gamma_\lambda^2)^{1/2}$ greater than the abscissa. The dashed curves represent the distribution expected if the reduced widths were drawn from Porter-Thomas distributions with no missed resonances. The solid curves are for 2, 5, and 14 missed resonances for $s_{1/2}, p_{1/2}$, and $p_{3/2}$, respectively.
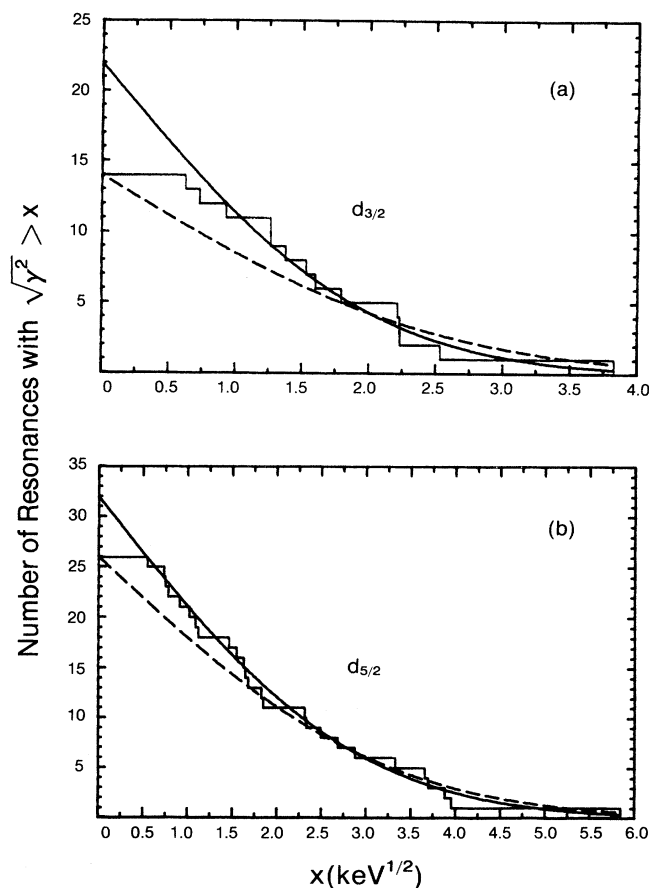
FIG. 7. Similar to Fig. 6 except for $d_{3/2}$ and $d_{5/2}$ resonances. The solid curves are for 8 missing $d_{3/2}$ and 6 missing $d_{5/2}$ resonances.

is identified at 664 keV. Above these lower-energy limits, we identify 14 $d_{3/2}$ resonances and 26 $d_{5/2}$ resonances. The Porter-Thomas test (see Fig. 7) indicates that 8, i.e., more than 50%, of the $d_{3/2}$ resonances are missing between 240 and 1500 keV. However, only 6 resonances are missing from the set of $d_{5/2}$ resonances observed above 660 keV.

An additional test for missing resonances and/or resonances for which incorrect (l,J) assignments have been made is provided by the Δ_3 test of Dyson and Mehta.[25] Up to neutron energy 110 keV the observed value of the Δ_3 statistic is consistent with no missed or spuriously identified resonances for the $s_{1/2}$ resonances. Inclusion of either or both the 11.181- and 17.97-keV resonances in the $s_{1/2}$ resonance set produces values of Δ_3 within one standard deviation of the expected value. Hence, either or both of these narrow resonances could be s wave, a re-

sult which disagrees with the $l=1$ assignment from earlier work.[7,22]

As is clear from Fig. 8, the observed level density for the $p_{1/2}$ resonances is markedly different above and below 600 keV. The values of Δ_3 over the two regions [175, 750 keV] and [600, 1200 keV] are both within one standard deviation of the expected Δ_3. However, the value for the entire region [175, 1200 keV] is much too large. A doorway[26] in the $p_{1/2}$ channel near 600 keV could produce such a dramatic change in the level density, but if that is the explanation then we would also expect a statistically significant increase in the $p_{1/2}$ strength function near the same energy. However, as will be discussed in Sec. VI C., no such increase is observed. Thus, we conclude that the smaller observed level density below 600 keV is simply due to resonances with widths too small to be identified in the present measurement. In fact, there are approximately 15 resonances below 175 keV with widths too small for the (l,J) assignments to be made. This interpretation will be reinforced in the discussion of the back-shifted Fermi-gas model of the observed $p_{1/2}$ level density.

We are missing many $p_{3/2}$ resonances. Inclusion of
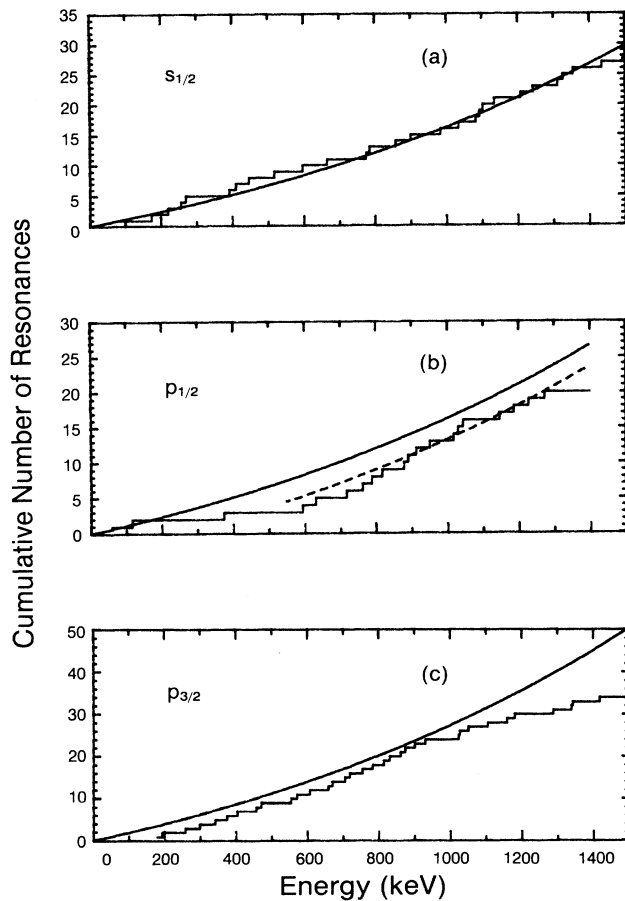
FIG. 8. The cumulative number of observed resonances versus neutron energy for $s_{1/2}$, $p_{1/2}$, and $p_{3/2}$ resonances. The curves are calculated using the back-shifted Fermi-gas model for the nuclear level density. The level density parameters $a_0 = 6.44$ MeV^{-1} and $U_0 = 0.76$ MeV were determined by fitting the total number of $s_{1/2}$ resonances from 10 to 1500 keV and the number of low-lying excited states in ^{41}Ar from 2.5 to 3.5 MeV above the ground state. The dashed curve in (b) is obtained by subtracting 3 resonances from the solid curve in (b).
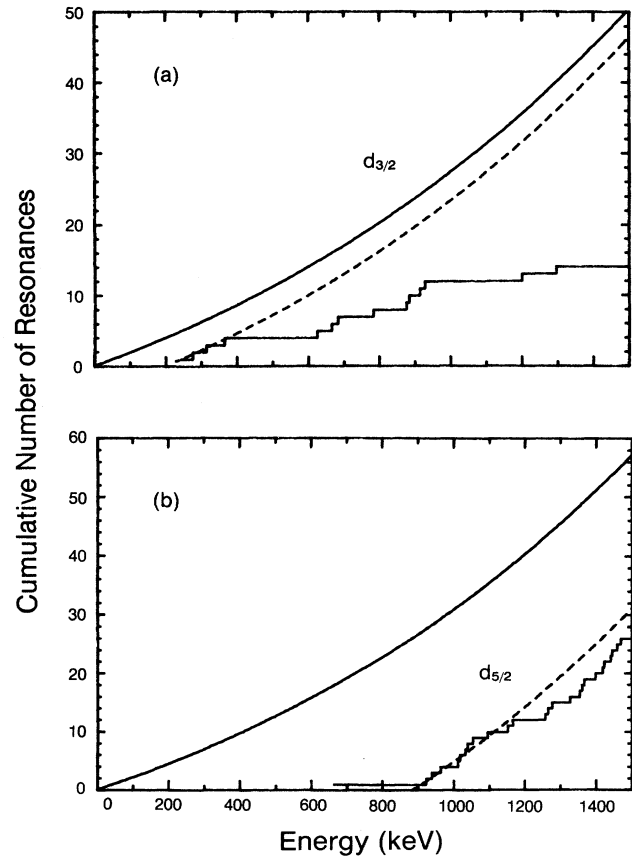
FIG. 9. Similar to Fig. 8 except for $d_{3/2}$ and $d_{5/2}$ resonances. The dashed curves are obtained by subtracting 4 and 26 resonances from the solid curves for $d_{3/2}$ and $d_{5/2}$ resonances, respectively.

both or either of the 11- and 18- keV resonances does not produce a value of Δ_3 within one standard deviation of the expected value over any interval beginning below 10 keV and extending to high enough energy to include at least 5 or 6 resonances. It is interesting, however, that the value of Δ_3 over the interval [175, 800 keV] is consistent with no missed or spuriously identified $p_{3/2}$ resonances. As will be discussed below, the back-shifted Fermi-gas model does provide a very good description of the observed $p_{3/2}$ level density over the region [200, 800 keV]. These results suggest that most of the missing $p_{3/2}$ resonances are probably lower in energy than 200 keV or above 800 keV.

The Dyson-Mehta Δ_3 test implies missing and/or spuriously identified $d_{3/2}$ resonances above 240 keV and $d_{5/2}$ resonances above 650.

In Table III are listed the observed number of resonances N_{lJ}^{obs}, our estimate of the number of missed levels N_{lJ}^m, and the average resonance spacings D_{lJ} defined by

$$D_{lJ} = (E_{\lambda f} - E_{\lambda i})/(N_{lJ}^{\text{obs}} + N_{lJ}^m - 1) , \qquad (6.1)$$

where $E_{\lambda i}$ and $E_{\lambda f}$ are the energies of the lowest- and highest-energy resonances in (l,J) data set. The ratio of the $p_{1/2}$ mean level spacing to that of the $p_{3/2}$ is 1.9 ± 0.2, consistent with the ratio expected for a $2J+1$ dependence of the level spacings on J.

B. Level densities

The density of resonances of given J, $\rho_J(E)$, is expected to display a noticeable curvature over the 1.5-MeV energy interval above neutron binding. In Figs. 8 and 9 are shown the observed cumulative number of resonances over the energy range of this measurement for the $\frac{1}{2}^+$, $\frac{1}{2}^-$, $\frac{3}{2}^-$, $\frac{3}{2}^+$, and $\frac{5}{2}^+$ resonances. The curvature indicating an increasing density of resonances is obvious in each data set except for the $\frac{3}{2}^+$ resonances. Of course, for the higher partial waves, some of the observed increase in density with energy is a result of the increase in neutron widths with energy. Historically, the determination of the energy dependence of the level density has been difficult because a large number of resonances with small widths were either not observed or their (l,J) assignments could not be made.

Since we seem to be missing only two resonances for the $s_{1/2}$ data set, that set can serve to determine the two level density parameters, a_0 and U_0, appearing in the back-shifted Fermi-gas model[27−31] of resonance density. This model represents the energy dependence of the density of levels, summed over l and J, as

$$\rho_{\text{tot}}(U) = \frac{1}{12\sqrt{2}\sigma} \frac{\exp[-2(a_0 U)^{1/2}]}{a_0^{1/4} U^{5/4}} . \qquad (6.2)$$

The excitation energy U is calculated relative to a fictive ground-state energy U_0 and is given by

$$U = E + (S_n - U_0) , \qquad (6.3)$$

where S_n is the neutron separation energy for $n + {}^{40}\text{Ar}$,

i.e., 6.099 MeV. The density of resonances for a given J is

$$\rho_J(U) = \rho_{\text{tot}}(U) \frac{(2J+1)\exp[-(J+\frac{1}{2})^2/2\sigma^2]}{2\sigma^2} . \qquad (6.4)$$

The energy dependence of the spin cutoff factor σ^2 is modeled as

$$\sigma^2 = 0.0888(A+1)^{2/3}(a_0 U)^{1/2} , \qquad (6.5)$$

where $A+1$ is the mass of the compound nucleus. The constant 0.0888 in Eq. (6.5) corresponds to modeling the fermi gas as composed of nuclei with a moment of inertia 75% that of a rigid rotator. The two parameters a_0 and U_0 are adjusted to give a good description of both the observed $s_{1/2}$ cumulative resonance distribution (corrected for 2 missing resonances) in the 1.275-MeV interval above neutron binding and the 12 observed[32] bound states in ${}^{41}\text{Ar}$ between excitation energies 2.5 and 3.5 MeV, high enough in excitation energy to avoid collective effects. Thus the parameters a_0 and U_0 are least-squares adjusted to satisfy

$$N^{\text{ex}} = \int dU \, \rho_{\text{tot}}(U) = 12 \qquad (6.6)$$

and

$$N(\tfrac{1}{2}^+) = \tfrac{1}{2} \int dU \, \rho_{1/2}(U) = 30 , \qquad (6.7)$$

where the integrations are from 2.5 to 3.5 MeV above the ground state for N^{ex} and from 0 to 1.5 MeV incident neutron energy for $N(\tfrac{1}{2}^+)$. The factor $\frac{1}{2}$ in Eq. (6.7) results from the assumption that both parities for a given J are equally represented. We find

$$a_0 = 6.44 \text{ MeV}^{-1} \qquad (6.8)$$

and

$$U_0 = 0.76 \text{ MeV} . \qquad (6.9)$$

The resulting calculated cumulated number of $s_{1/2}$ resonances is shown as a solid curve in Fig. 8(a).

Given the parameters a_0 and U_0, the back-shifted Fermi-gas model can be used to predict the cumulative number of resonances expected for the $\frac{1}{2}^-$, $\frac{3}{2}^-$, $\frac{3}{2}^+$, and $\frac{5}{2}^+$ resonances. These predictions are shown as the solid curves in Figs. 8(b), 8(b), and 9. For the $\frac{1}{2}^-$ resonances the model predicts about 3 or 4 more resonances than are observed between 10 and 600 keV. Above 600 keV, the slope of the calculated cumulative number of resonances [solid curve in Fig. 8(b)] is essentially that which is observed. The dashed curve in Fig. 8(b) results from subtracting 3 resonances from the calculated distribution. The Fermi-gas model seems consistent with about three missing $p_{1/2}$ resonances below 600 keV and perhaps as many as two missed resonances above 1300 keV where we are able to identify no $p_{1/2}$ resonances. These results are consistent with the statistical tests discussed in the preceding section.

Again using the values of a_0 and U_0 derived from the

$s_{1/2}$ resonance set, the back-shifted Fermi-gas model overpredicts the cumulative number of $p_{3/2}$ resonances over the entire experimental range [see Fig. 8(c)]. In fact, even in the first 100-keV interval, there already appears to be 2 or 3 missing $p_{3/2}$ resonances. The slope, i.e., the resonance density, of the calculated cumulative distribution in Fig. 8(c) is very nearly that observed over the interval [200, 800 keV], the same region which produces a value of Δ_3 consistent with no spuriously assigned $p_{3/2}$ resonances. Thus most of the missing $p_{3/2}$ resonances appear to be in the intervals below 200 keV and above 800 keV.

The observed cumulative number of $d_{3/2}$ resonances [see Fig. 9(a)] increases much more slowly than does the calculated distribution using the Fermi-gas model parameters determined from the $s_{1/2}$ resonance set. Over the interval 240 to 1500 keV the model predicts 44 $d_{3/2}$ resonances while we identify only 14. Likewise the model predicts 40 $d_{5/2}$ resonances above 650 keV, whereas we identify only 26. However, in the case of the $d_{5/2}$ resonances, the slope of the calculated cumulative number of resonances in Fig. 9(b) is in good agreement with that observed. The dashed curve in Fig. 9(b) is the result of subtracting 17 resonances from the calculated cumulated distribution.

The work on level densities by Gilbert and Cameron[29] gave $a_0 = 5.74$ MeV^{-1} for mass region near $A = 40$, in poor agreement with our result. However, the comparison is compromised because a composite level density rather than a simple back-shifted model was used by Gilbert and Cameron. In a later study of resonance densities, Dilg et al.[30] used the back-shifted Fermi-gas model but with different values for the spin cutoff factor σ^2 and hence a simple comparison is not possible. Dilg et al. considered two values for σ^2, one corresponding to treating the compound nucleus as having a moment of inertia, I_{rigid}, of a rigid body and the other having $\frac{1}{2}$ that moment. The value we use corresponds to treating the compound nucleus as having a moment equal to $0.75I_{\text{rigid}}$. The two values reported by Dilg et al.[30] are $(a_0, U_0) = (4.52$ MeV^{-1}, -0.96 MeV), treating the compound nucleus as having moment of inertia $I = 0.5I_{\text{rigid}}$, and $(a_0, U_0) = (5.48$ MeV^{-1}, -0.49 MeV) for $I = I_{\text{rigid}}$. The value for a_0 from our analysis is considerably larger than either of the values reported by Dilg et al.[30] Moreover, not only is the magnitude of the fictive ground-state energy, U_0, from our analysis twice that of Dilg et al.,[30] the sign of U_0 is opposite to theirs. The model of Dilg et al.[30] using $I = I_{\text{rigid}}$ underestimates the cumulative number of $s_{1/2}$ resonances over $[E_1, E_2]$ by 5 resonances; moreover, their model overpredicts the bound-state density by a factor of two. Adjustment of U_0 to 0.2 MeV in their model, a value more nearly consistent with that from our work, results in better agreement between observation and the model for the bound-state density but underpredicts the observed $s_{1/2}$ cumulative distribution by about 30%. A recent discussion of statistical properties of excited nuclear states by Ignatyuk[31] gives a value of about 6 MeV^{-1} for nuclei near mass 40, consistent with the value from our work.

C. Strength functions

The observed neutron strength functions s_{lJ} are defined as

$$s_{lJ} = \frac{\langle \gamma^2_{\lambda lJ} \rangle}{D_{lJ}} = \frac{N^{\text{obs}} - 1}{N^{\text{obs}}} \frac{\sum_\lambda \gamma^2_{\lambda lJ}}{\Delta E_{lJ}} , \tag{6.10}$$

where the ΔE_{lJ} are the energy intervals between the lowest- and highest-energy resonances of type (l, J). The angle-bracket notation in Eq. (6.10) indicates the averaging process. The s_{lJ} are very nearly the slopes of the cumulative reduced width versus energy distributions shown in Figs. 10 and 11 for $s_{1/2}$, $p_{1/2}$, $p_{3/2}$, $d_{3/2}$, $d_{5/2}$, and d-wave resonances. The s-wave strength function derived from this work is energy-dependent and is well represented by Eq. (4.8). The parameters α_{lJ} and β_{lJ} were determined by fitting the observed cumulative distributions and are given in Table III. The resulting functions are shown as solid curves in Figs. 10 and 11.

The observed strength functions should be corrected for the effects of missed resonances. However, in the present work these corrections are negligible. For exam-
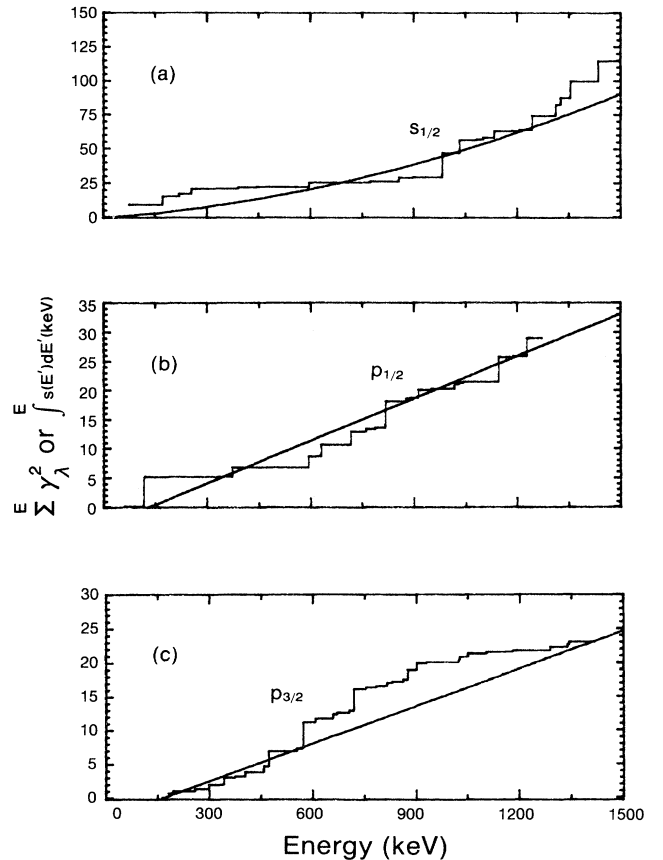
FIG. 10. Cumulative reduced widths for s- and p-wave resonances. The histograms show the summation of observed reduced widths and the curves are least-squares fits of the integral of the strength, Eq. (4.8), to the histograms. The resulting values of the parameters α_{lJ} and β_{lJ} are listed in Table III.

ple, in the case of the $p_{3/2}$ resonances, if the missing 14 resonances are assumed to have reduced widths no larger than the smallest observed $p_{3/2}$ reduced width, the correction to the observed slope is less than 2%. Since these corrections are very small and are rather uncertain, we make no corrections to the observed cumulative width distributions for the effects of missing resonances.

Presented in Fig. 11(c) is the cumulative d-wave reduced neutron width distribution weighted by the statistical weight factor $g(J)$. The slope of this curve is the d-wave strength function defined as

$$s_{l=2} = \tfrac{1}{5} \sum_\lambda g(J) \gamma_{lJ\lambda}^2 / \Delta E_{l=2} , \tag{6.11}$$

where the interval $\Delta E_{l=2} = 1518 - 243$ keV. The resulting d-wave strength function is 0.095 ± 0.022. No attempt is made to correct for missed d-wave resonances.

D. Conventionally defined strength functions

The strength function which has been most often reported[22] in the earlier literature is the ratio

$$S_{lJ} = \langle \Gamma_{nJ}^l \rangle / D_{lJ} , \tag{6.12}$$

where the Γ_{nJ}^l are the conventionally reduced widths,

$$\Gamma_{nJ}^l = \left[\frac{1 \text{ eV}}{E_{\lambda lJ}} \right]^{1/2} \frac{\Gamma_{\lambda J}}{v_l} \tag{6.13}$$

and the v_l are the neutron penetration factors[22] for partial waves with orbital angular momenta l. The S_{lJ} are proportional to the strength functions s_{lJ} given in the preceding section, i.e.,

$$S_{lJ} = (4.39 \times 10^{-4})(A / A + 1) a_c s_{lJ} , \tag{6.14}$$

where $a_c = 5.0$ fm in this work. The relationship between S_{lJ} and s_{lJ} is discussed more fully by Carlton et al.[19] Use of definition [Eq. (6.14)] does produce a quantity which for s-wave neutrons at low energies is independent of the boundary radius, a_c. For higher l waves and, even for s waves at higher energies, the S_{lJ} are functions of a_c. Even so, for the earlier work at energies below 100 keV or so, the S_{lJ} were useful quantities since comparisons

FIG. 11. Similar to Fig. 10 except for $d_{3/2}$ and $d_{5/2}$ resonances. Panel 10(c) represents the cumulative d-wave $g(J)\gamma_\lambda^2$ and the corresponding d-wave strength function.
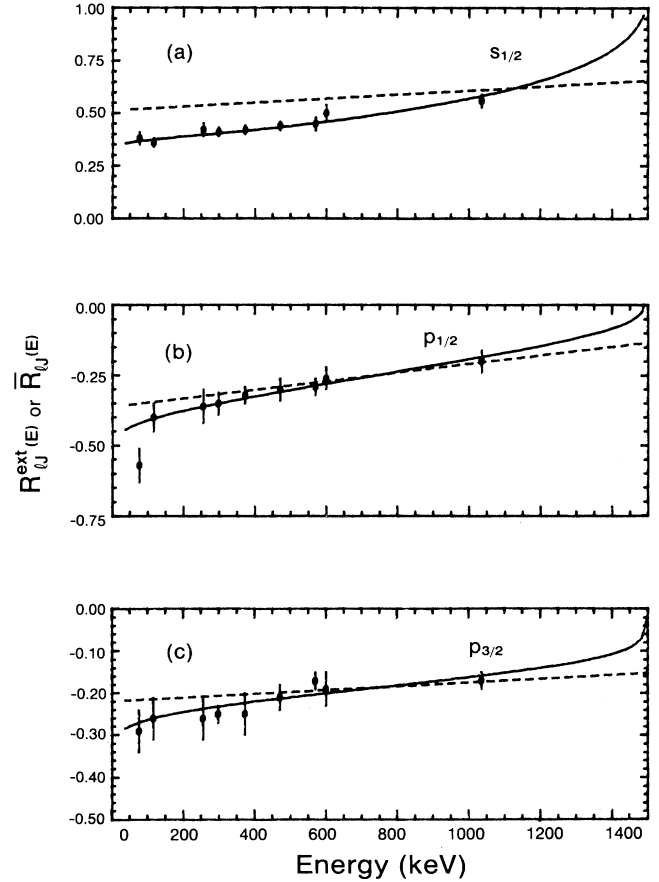
FIG. 12. Empirical external R functions R_{lJ}^{ext} (solid curves), deduced from the R-matrix analysis, and the corresponding smoothed R functions, $\overline{R}$ (dashed curves) for $s_{1/2}, p_{1/2}$, and $p_{3/2}$. The curves represent Eqs. (4.7), (4.8), and (4.9) using the optimal values of α_{lJ}, β_{lJ}, a_{lJ}, and b_{lJ} as listed in Table III. The error bars were determined by varying the optimal values of a_{lJ} and b_{lJ} until noticeable degradation of the quality of the fits was observed.

with optical model calculations of $S_{l=0,J}$ could be made without regard to the value of a_c used in either the data analysis or the optical model calculations. The value of the conventionally defined s-wave strength function, evaluated at 500 keV,

$$S_{l=0,1/2} = (0.42 \pm 0.12) \times 10^{-4} , \tag{6.15}$$

derived from the present work is barely consistent with that from earlier measurements,[7]

$$S_{l=0,1/2} = (0.91^{+0.77}_{-0.37}) \times 10^{-4} . \tag{6.16}$$

Earlier work could not resolve the two J values for the p-wave resonances and hence only a p-wave strength function

$$S_{l=1} = \tfrac{1}{3} \sum_J g(J) \Gamma^{l=1}_{\lambda J} / \Delta E_{l=1} \tag{6.17}$$

was reported,[7] $S_{l=1} = (0.35 \pm 0.11) \times 10^{-4}$. The present work yields

$$S_{l=1} = (0.39 \pm 0.07) \times 10^{-4} , \tag{6.18}$$

in excellent agreement with the earlier work. In these conventionally defined units, the d-wave strength function is

$$S_{l=2} = (2.0 \pm 0.5) \times 10^{-4} . \tag{6.19}$$

E. R functions

The data points in Fig. 12 represent the external R functions $R^{ext}_{lJ}(E)$ for s- and p-wave resonances. These data were obtained by careful examination of the cross section near isolated resonances for which the (l,J) assignments are unambiguous. The solid curves in Fig. 12 are the result of least-squares adjustment of the parameters α_{lJ} and β_{lJ} appearing in the expression [Eq. (4.9)] for $\overline{R}_{lJ}(E)$ with the parameters a_{lJ} and b_{lJ} taken from Table III. The resulting values of α_{lJ} and β_{lJ} are given in Table III. The uncertainties in R^{ext}_{lJ}, represented by vertical bars in Fig. 12, have been estimated from observed changes in the calculated resonance asymmetry and/or off-resonance cross section resulting from small changes in the parameters α_{lJ} and β_{lJ}. The smooth functions $\overline{R}_{lJ}(E)$ are shown as dashed curves in Fig. 12.

The s-wave potential scattering radius R' is determined from $\overline{R}_{l=0,1/2}(E)$ evaluated at $E=0$,

$$R' = a_c[1 - \overline{R}_{0,1/2}(0)] = 2.49 \text{ fm} , \tag{6.20}$$

in very good agreement with the result reported in earlier work,[22] $R' = 2.7 \pm 0.2$ fm. The value of R' is independent[19] of the channel radius a_c.

F. The average scattering functions

To a good approximation,[16−18] the scattering functions $\langle S_{lJ}(E) \rangle$ can be expressed in terms of the smooth R function, $\overline{R}_{lJ}(E)$, and the strength function, $s_{lJ}(E)$, as

$$\langle S_{lJ}(E) \rangle = e^{2i\phi_l(E)} \frac{[1 + iP_l(E)R_{lJ}(E)]}{[1 - iP_l(E)R_{lJ}(E)]} , \tag{6.21}$$

where

$$R_{lJ}(E) = \overline{R}_{lJ}(E) + i\pi s_{lJ}(E) . \tag{6.22}$$

The empirical functions $\overline{R}_{lJ}(E)$ and $s_{lJ}(E)$ play dual roles in determining $\langle S_{lJ}(E) \rangle$; both functions are required[1−6] to determine both the real and imaginary parts of the averaging scattering function.

VII. CONCLUSIONS

We have measured neutron transmission for ^{40}Ar from 10 keV to 50 meV. From these data our R-matrix analysis provides strength and external R functions and resonance densities from just above neutron binding in the $n + ^{40}$Ar system to the inelastic neutron-scattering threshold at ~ 1.5 MeV. These data are sufficient to provide a detailed description of the scattering matrix for the $s_{1/2}$, $p_{1/2}$, and $p_{3/2}$ scattering channels from 10 keV to 1.5 MeV. Beyond 1.5 MeV our measurements yield averaged neutron total cross sections up to 50 MeV. These average scattering functions and average cross sections can be described by a dispersive optical model. Since relatively few s- and p-wave resonances are missed in the present work, the observed resonance densities in these three channels provide information about the energy dependence of the level densities as described using the back-shifted Fermi-gas model.

ACKNOWLEDGMENTS

[1]C. Mahaux and H. Ngo, Nucl. Phys. A **378**, 205 (1982).

[2]C. H. Johnson and C. Mahaux, Phys. Rev. C **38**, 2589 (1988).

[3]J. P. Delaroche, Y. Wang, and J. Rapaport, Phys. Rev. C **39**, 591 (1989).

[4]C. H. Johnson, D. J. Horen, and C. Mahaux, Phys. Rev. C **36**, 2252 (1987).

[5]C. H. Johnson and R. R. Winters, Phys. Rev. C **37**, 2340 (1988).

[6]C. H. Johnson, R. F. Carlton, and R. R. Winters, Phys. Rev. C **39**, 415 (1989).

[7]H. I. Liou, J. Rainwater, G. Hacken, and U. N. Singh, Phys. Rev. C **11**, 457 (1975).

[8]F. T. Seibel, Ph.D. dissertation, Duke University 1968 (unpublished).

[9]J. A. Harvey and N. W. Hill, Nucl. Instrum. Methods **162**, 507 (1979).

[10]C. M. Perey, J. A. Harvey, R. L. Macklin, F. G. Perey, and R. R. Winters, Phys. Rev. C **27**, 2556 (1983).

[11]D. C. Larson, N. M. Larson, and J. A. Harvey, Oak Ridge National Laboratory Report ORNL/TM-8880, 1984 (unpublished).

[12]D. C. Larson, N. M. Larson, J. A. Harvey, N. W. Hill, and C. H. Johnson, Oak Ridge National Laboratory Report ORNL/TM-8203, 1983 and Report ENDF-333, 1983 (unpublished).

[13]C. Coceva, R. Simonini, and D. K. Olsen, Nucl. Instrum. Methods **221**, 459 (1983).

[14]A. Smith, P. Guenther, D. Smith, and J. Whalen, Nucl. Sci. Eng. **72**, 293 (1979).

[15]A. M. Lane and R. G. Thomas, Rev. Mod. Phys. **30**, 257 (1958).

[16]C. H. Johnson, N. M. Larson, C. Mahaux, and R. R. Winters, Phys. Rev. C **31**, 1563 (1984).

[17]C. H. Johnson, C. Mahaux, and R. R. Winters, Phys. Rev. C **32**, 1359 (1985).

[18]C. H. Johnson and R. R. Winters, Phys. Rev. C **21**, 2190 (1980).

[19]R. F. Carlton, R. R. Winters, C. H. Johnson, N. W. Hill, and J. A. Harvey, Phys. Rev. C **38**, 1605 (1988).

[20]N. M. Larson and F. G. Perey, Oak Ridge National Laboratory Report ORNL/TM-7485, 1980 and Report ENDF-297, 1980 (unpublished).

[21]G. F. Auchampauch, Los Alamos Scientific Laboratory Report LA-5473-MS, 1974 (unpublished).

[22]S. F. Mughabghab, *Neutron Cross Sections* (Academic, New York, 1984), Vol. 1.

[23]C. E. Porter and R. G. Thomas, Phys. Rev. **104**, 483 (1956).

[24]M. S. Moore, J. D. Moses, and G. A. Keyworth, Phys. Rev. C **18**, 1328 (1978).

[25]F. J. Dyson and M. L. Mehta, J. Math. Phys. **4**, 489 (1963).

[26]B. Block and H. Feshbach, Ann. Phys. (N.Y.) **23**, 47 (1963).

[27]H. A. Bethe, Rev. Mod. Phys. **9**, 69 (1937).

[28]E. Erba, U. Facchini, and E. Saetta-Menichella, Nuovo Cimento **22**, 1237 (1961).

[29]A. Gilbert and A. G. W. Cameron, Can. J. Phys. **43**, 1446 (1965).

[30]W. Dilg, W. Schantl, H. Vonach, and M. Uhl, Nucl. Phys. **A217**, 269 (1973).

[31]A. V. Ignatyuk, Report Trans. IAEA, INDC(CCP)-233/L, 1985.

[32]*Table of Isotopes,* 7th Ed., edited by C. M. Lederer and V. S. Shirley (Wiley, New York, 1978).